note finali coverpage

24/10/2023 10:25

(Article begins on next page)

1   **Liquefaction source layer for sand blows induced by the 2016 megathrust earthquake (Mw**

2   **7.8) in Ecuador (Boca de Briceño)**

3

4   Aura C. Salocchi[a], Luca Minarelli[b], Stefano Lugli[a], Sara Amoroso[b, c], Kyle M. Rollins[d], Daniela

5   Fontana[a*]

6

7   a Department of Chemical and Geological Sciences, University of Modena and Reggio Emilia,

8   41125 Modena, Italy

9   b Istituto Nazionale di Geofisica e Vulcanologia, 67100 L'Aquila, Italy.

10   c Department of Engineering and Geology, University of Chieti-Pescara, 65129 Pescara, Italy

11   d Department of Civil and Environmental Engineering, Brigham Young University, UT 84602,

12   USA.

13   * corresponding author, daniela.fontana@unimore.it

14

15

16   **Abstract**

17   Numerous sand boils were generated in the alluvial plain at the mouth of the Rio Briceño valley

18   (Ecuador) during the Mw 7.8 earthquake of April 2016. The area is characterized by a series of

19   raised marine terraces formed as a consequence of the rapid tectonic coastal uplift during the

20   Quaternary. On the basis of boreholes and geognostic investigations carried out within a mitigation

21   project for liquefaction below a highway embankment and during post-earthquake surveys, we

22   recognized 5 lithological units in the subsurface, reflecting the continental-marine and transitional

23   sedimentation since the Last Glacial Maximum. We performed a comprehensive study of texture

24   and petrographic composition of sand boils compared with sandy silts and silty sands of the buried

25   sedimentary sequence in order to identify the source levels for liquefaction. The petrographic

26   components, in particular the low content of bioclasts and carbonate fragments of the sand boils,

27   allow to pinpoint a source layer made up of fine-grained silty sands located between 2 and 4.5 m

28   depth (unit 2) whereas the deeper marine sands, richer in bioclasts, were not involved. The results

29   support the idea that earthquake-induced liquefaction phenomena are not restricted to clean sands

30   and well-sorted deposits, but may affect sand layers with significant amount of non-plastic silt.

31

34

1. Introduction

Several liquefaction phenomena occurred as a consequence of a strong earthquake (M_w7.8) of April 2016 along the central Pacific coastline of Ecuador (GEER-ACT, 2016; Chunga et al., 2017). The earthquake was located onshore, less than 10 km southeast of the city of Pedernales, with a hypocentral depth of 21 km, rupturing the central seismogenetic segment of the South American subduction zone. In this area, the study of the liquefaction phenomena is particularly significant because frequent and very strong earthquakes are generated by megathrusts in a geological context characterized by continuous uplift and high sedimentation rate providing a complex stratigraphic architecture. In particular, the sediments involved in the liquefaction phenomena belong to the high-frequency sedimentary cycles related to the Quaternary climatic oscillations, which are extremely well recorded in the marine-continental successions. Moreover, the study of liquefaction effects is particularly relevant considering that these coastal areas contain urban centres, infrastructure and communication networks, that were recently the object of innovative mitigation strategies (Smith and Wissmann 2018, Vera-Grunauer et al. 2019, Amoroso et al. 2020a).

The aim of this research is to define the stratigraphic architecture of the shallow subsurface of the Boca de Briceño area in order to identify the source levels for liquefaction, using the texture and composition of sand boils compared with the buried sedimentary sequence. The study also may provide insights into ejection mechanisms in regions impacted by frequent earthquakes that triggered recurrent liquefaction (Giona Bucci et al., 2018; Maurer et al., 2019) and contribute in evaluating the success of a mitigation project carried out below a highway embankment in this area.

2. Geological setting

The study area is located on the coast of mainland Ecuador, a zone of intense crustal deformation due to the subduction of the Nazca oceanic plate beneath the South-American continental plate (Fig. 1). The subduction occurs along a N90°E direction at a rate of 58-78 mm/a (Trenkamp et al., 2002). The subduction induces a shortening perpendicular to the trench axis and, in turn, the expulsion of the north Andean block to the Northeast along the Guayaquil Caracas Megashear, with a rate of ~6 to 10 mm/a (Kellogg and Vega, 1995; Ego et al., 1996; Trenkamp et al., 2002). Recently, before the 2016 earthquake (M_w 7.8), the Ecuadorian shoreline experienced strong megathrust earthquakes: in 1906 (estimated Mw 8.8, 600-km long rupture area, one of the strongest earthquake registered on our planet), 1942 (M_w 7.8), 1958 (M_w 7.7), and 1979 (M_w 8.2).
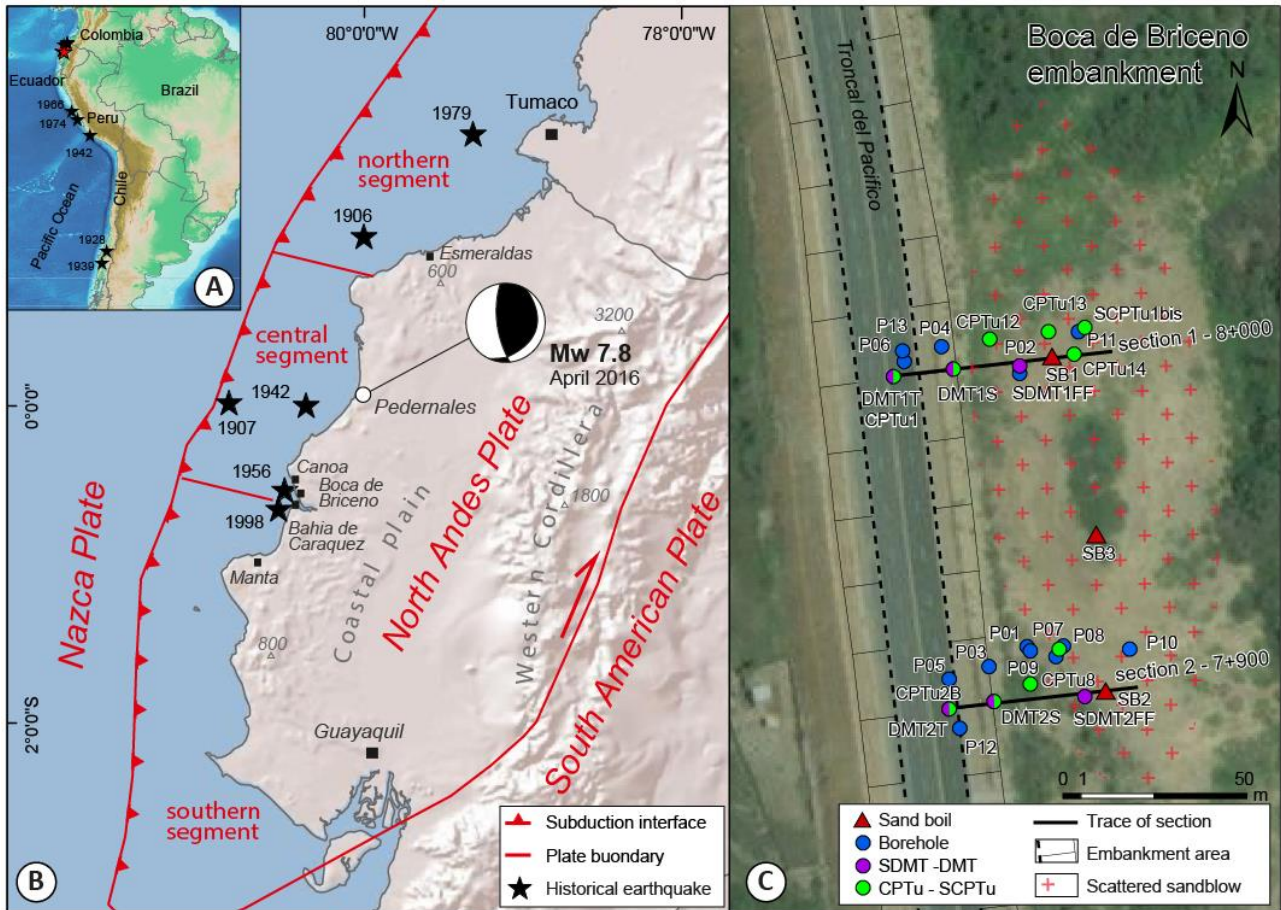
Fig. 1 Location (A) and seismotectonic map (B) of the Briceño Bridge area in Ecuador with indication of the historical earthquakes (modified after Amoroso et al., 2020 and Chunga et al. 2018). Study area with location of sand blows and boreholes (C).

The Colombia–Ecuador subduction trench is characterized by rapid sedimentation due to a tropical climate and orographic rains on the western Andean slope caused by the prevailing Pacific winds. The trench contains a thick sedimentary infill, up to 3 km-thick, probably due to recent turbidites associated with hemipelagic sedimentation. The high sediment thickness along the subducting margin seems to influence the large ruptures associated with great megathrust earthquakes. The subduction of large volumes of sediments creates a sort of homogenous plate interface, which allows the seismic ruptures to overcome the bathymetric barriers, propagating the trench-parallel ruptures (Alvarez et al., 2017).

The Ecuadorian margin substratum consists of the oceanic North-Andean block accreted to the Brazilian continental craton during the Cretaceous (Jaillard et al., 1997). The oceanic terranes are made up of tholeiitic-andesitic basalts and pillow lavas associated with siliceous sediments (Piñon Formation) overlain by intra-oceanic volcanic arc sequences (Cayo formation, Jaillard et al., 1995; Reynaud et al., 1999).

The coastal area of Ecuador (Talara Arc) is actively uplifted along a concave subduction zone. The uplift is related to the eastward subduction of the aseismic Carnegie Ridge, which is part of the oceanic Nazca plate. The active subduction of the ridge is responsible for great lateral variations in deformation, seismicity, magmatism and sediment deposition along the margin (Gutscher et al., 1999; Collot et al., 2002). The uplift rate in the coastal area of Ecuador ranges between 0.10 and 0.42 mm/a for the Late Quaternary (Pedoja et al., 2006). As a result of the rapid uplift, the coast is characterized by well-preserved, raised, marine terraces, called Tablazos, which show late Pliocene to Pleistocene high-frequency depositional sequences (Cantalamessa et al., 2001; Di Celma et al., 2002).
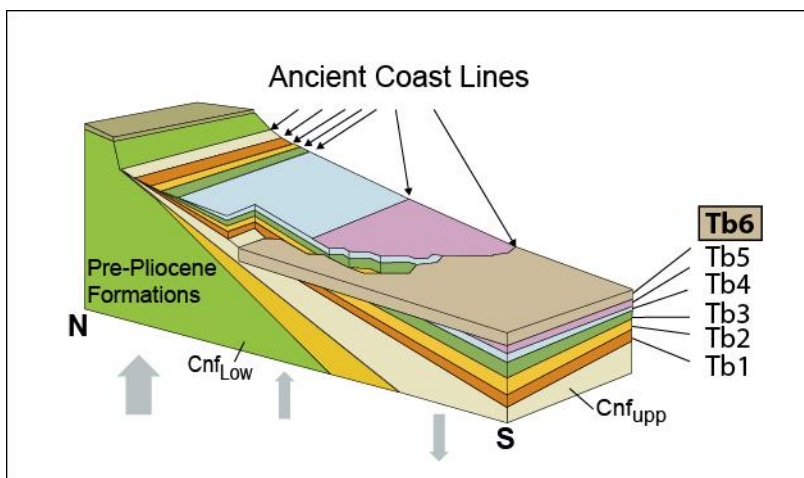
Fig. 2 Block diagram illustrating the Plio-Pleistocene stratigraphic architecture of costal Ecuador according to Cantalamessa and Di Celma (2004). CnF$_{low}$: lower Canoa Formation, CnF$_{upp}$: upper Canoa Formation. Tb: Cyclothems of the Tablazo Formation. The studied succession belongs to the Tb6 sequence.

2.1 The sedimentary sequence of the coastal margin

The combined effects of tectonic coastal uplift and Quaternary sea level fluctuations resulted in the formation of a series of raised marine terraces on the coastal stretch of mainland Ecuador. The Pliocene-Pleistocene coastal sequence was traditionally subdivided into the Canoa Formation and the Tablazo Formation (Sheppard, 1930). Di Celma et al. (2002) and Cantalamessa and Di Celma (2004) recognized up to four marine terraces in the area, while Pedoja et al. (2006) mapped up to five terraces. The significance of the terraces for the interpretation of the uplift rates of coastal Ecuador was stressed by Pedoja et al. (2006a, 2006b) and the cyclothemic nature of these formations was described in detail by Di Celma et al. (2002), Cantalamessa and Di Celma (2004). According to Cantalamessa and Di Celma (2004), the sedimentary succession lies unconformably on pre-Pliocene deposits and reflects deposition in offshore, shoreface, and alluvial environments

(Fig. 2). The cyclothem consists of a deepening–shallowing upward facies association bounded by a ravinement surface, amalgamated with the preexisting sequence boundary. Each of the marine terraces formed during sea-level rise and highstand, and was progressively uplifted during a cycle of sea-level fluctuation. The terraces are composed of a wave-cut platform formed during the transgressive stage, covered by thin beach deposits consisting of sands, pebbles and shell fragments. The Canoa Formation lies unconformably over the Tosagua Formation (Early Miocene) and has been divided into two units with different deepening–shallowing facies associations, CnF_{low} (late Pliocene) and CnF_{upp} (Early Pleistocene), separated by an angular unconformity. The Tablazo Formation (Middle Pleistocene–Holocene) consists of at least six cyclothems characterized by a deepening–shallowing facies sequence. The cyclothems represent a single forced regressive sequence set.

Only in the last cyclothem (sequence Tb6, Fig. 2) the shallowing-upward part of the depositional sequence can be seen, differently from the lower cyclothems where the corresponding part of the sequence was eroded during the ravinement surface formation at each sequence boundary. Sequence Tb6 begins with a ravinement surface followed by a transgressive, deepening-upward shoreface succession, capped by a shallowing-upward shoreface to coastal-plain facies succession. In correspondence of the main fluvial entry points, the sequence is cut by valleys filled by estuarine sediments. The alluvial-estuarine deposits may contain Late Pleistocene–early Holocene continental vertebrate (Cantalamessa et al., 2001). The fluvial valleys, cut during sea level lowstands, were flooded and filled during the early phase of the Holocene transgression. As a whole, the depositional sequence seems to reflect the last cycle of sea-level fluctuation since MIS 5e, and represents the result of the sedimentation of the last 124 ka.

2.2 The Boca de Briceño area

The area is characterized by Mio-Pleistocene turbidite deposits and Quaternary alluvial and marine terraces consisting of gravels, sand, silt and clay, highly variable in thickness and lateral extent, cut by the Rio Briceño valley. Detailed post-earthquake surveys were performed to detect the numerous site effects developed in the area, as well as along the Ecuadorean coast (GEER-ACT 2016, Chunga et al. 2017). In particular, liquefaction phenomena were observed and studied at the Briceño embankment, approximately 7 km from Canoa city and 112 km from the earthquake epicenter (Fig. 1b). The estimated peak ground acceleration at the site was 0.4g (Ye et al., 2016, Beauval et al., 2017).

The earthquake shaking generated numerous sand boils in the alluvial plain (Fig. 1c), clustering in a wide elongated area next to the river mouth, a few hundreds of meters from the shoreline (Fig. 1c).

148 Sand boils were generally small, about 1 m across and a few centimetres high, and grew above a
149 flat surface cut by mud cracks (Fig. 3).
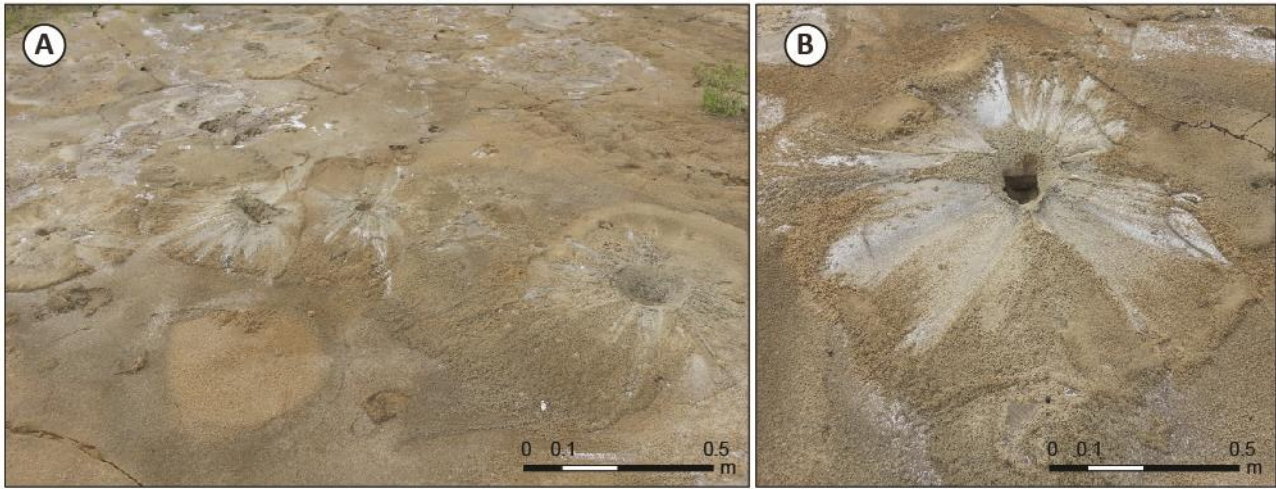
151 **Fig. 3** Sand boils in the Briceño Bridge area photographed after the main shock, a few months later
152 (A), and detail of a sand volcano (B).

154 As shown in Fig 1c, the sand boils are located in the area adjacent to the embankment, next to the
155 bridge abutment, along the the Troncal de Pacifico Road. This infrastructure exhibited minimal
156 damage due to the earthquake (GEER-ACT, 2016), likely as a result of a mitigation project to
157 prevent liquefaction-induced failures (Smith and Wissmann 2018). Rammed aggregate pier®
158 (RAP) ground improvement elements were used to reinforce foundation materials and to increase
159 the stability of the sand deposits in the subsurface, which has been used successfully at similar sites
160 in New Zealand (Wissmann et al., 2015 ; Wentz et al., 2015 ; Vauther in et al., 2017) and in Italy
161 (Amoroso et al., 2020b).

162 In this context, an extensive geological and geotechnical site characterization campaign was
163 performed mostly along two sections of the Briceño bridge embankment, with the aim of
164 examining in depth the mechanisms involved in the liquefaction processes and evaluation of
165 mitigation effectiveness (Smith and Wissmann, 2018; Amoroso et al., 2020a).

3. Methods and sampling

169 To reconstruct the stratigraphy of the area (Fig. 4), we based our observations on the complete
170 dataset acquired during the mitigation project and subsequent post-earthquake investigations (Smith
171 and Wissmann, 2018; Amoroso et al., 2020a). In particular we examined in detail cores from 13
172 boreholes: five log cores (P07, P08, P09, P10, P11) to a depth of 6 m, five log cores 12 m deep (P02
173 starting from the ground level and P03, P04, P05, P06 starting from the bridge embankment) and
174 one core to a depth of 30 m (P01). The stratigraphic observations were supplemented by

175 geotechnical data consisting of standard penetration test (SPT), Atterberg limits, 16 piezocone tests

176 (CPTu), 4 seismic piezocone tests (SCPTu), 5 flat dilatometer tests (DMT) and 2 seismic

177 dilatometer tests (SDMT). The location of cores and other investigations is reported in Fig. 1c.

178 Four boreholes (P07, P09, P10, P11) were sampled for textural (grain size) and compositional

179 analyses (Fig. 4). The same textural and petrographic analyses were carried out on sand volcanoes

180 from three different sites (samples SB1, SB2, SB3; with locations reported in Fig 1c).

181 *Grain-Size Analyses.* We analyzed eighteen samples from cores P07, P09, P10, P11 at different

182 depths and from sand blows (Table 1, Fig. 5). Grain-size analyses were performed on the

183 Mastersizer 3000 Laser granulometry (Low Angle Laser Light Scattering) at laboratories of the

184 DSCG of the University of Modena and Reggio Emilia. Organic matter was removed from 80 g of

185 samples by hydrogen peroxide (H_2O_2); the samples were air dried and mechanically sieved for

186 granulometric and compositional analyses. About 0.5 g of sample were transferred into a 250 ml

187 beaker filled by deionized water. The suspension was lit by the low-intensity laser beam; particle-

188 size distribution data were obtained under constant agitation in the measuring beaker. A refractive

189 index of 1.52 for the laser radiation (λ =750 nm), an absorption coefficient of 0.1 and a Dispersal

190 Refractive Index of 1.33 for the total range were used. For each sample five measurements were

191 taken for three aliquots, then averaged. Index properties were estimated using the grain size

192 distribution, by means of the Atterberg limits, fines content (FC) which represents percentage of

193 particles finer than 0.075 mm; the diameters of the 60th (D_{60}), 30th (D_{30}), and 10th (D_{10}) percentile of

194 the granulometric curve; the coefficient of uniformity (U), given by the ratio between D_{60} and D_{10};

195 and the coefficient of curvature (C), function of D_{60}, D_{30}, and D_{10}.

196 *Compositional Analyses.* Point counting was performed on eleven samples under transmitted-light

197 microscopy on the 0.125–0.250 mm fraction, according to the Gazzi-Dickinson method designed to

198 minimize the dependence of the analysis on the grain size (Zuffa, 1985; Arribas and Tortosa, 2003).

199 We distinguished 23 compositional categories reported in Table 2. Results are plotted in the

200 traditional Q (quartz), F (feldspars), L (siliciclastic lithics) + C (carbonate) diagram (Fig. 6a) and

201 are shown also in the Q+F, L, C plot (Fig 6b) that makes it possible to better differentiate the

202 compositional fields in Quaternary sands, as discussed by Lugli et al. (2007).

203

204   4. **Results**

205

206 *4.1 The Boca de Briceño sedimentary sequence*

The studied sedimentary sequence can be divided into 5 main lithological units showing variable thickness. These units, detected in both sections of the bridge embankment shown in Fig. 4, are from the top to the bottom:

Unit 1, consisting of recent laminated silt and clayey silt with subordinate sandy layers, from the ground level to a depth ranging from 1.35 to 3.50 m; the unit locally fills paleochannels and may reach the depth of 5 m (section 1).

Unit 2, consisting of silty sands with rare seashell beds, with variable thickness within the studied area; the top of the unit ranges from 1.35 to 3.5 m depth, and its base from 3.8 to 5.50 m depth.

Unit 3 is very thin (maximum 1 m thick) and discontinuous, made up of clayey silt with subordinate sands, and it has been recognized only in the southern area (section 2 in Fig. 4) at the depth of 4 m.

Unit 4 consists mainly of coarse-grained sands and minor pebbles with abundant seashell beds. The top of the unit ranges from 3.8 to 5.50 m depth and the bottom from 9.00 m (P01) to more than 12 m depth (P02 hole bottom).

Unit 5, consists of compacted silty and clayey sediments with subordinate silty sands and widespread oxidation traces. The top of the unit is detected at a depth varying from 9.00 m to more than 12 m, and it extends down to a depth of 28.65 m (P01 hole bottom).
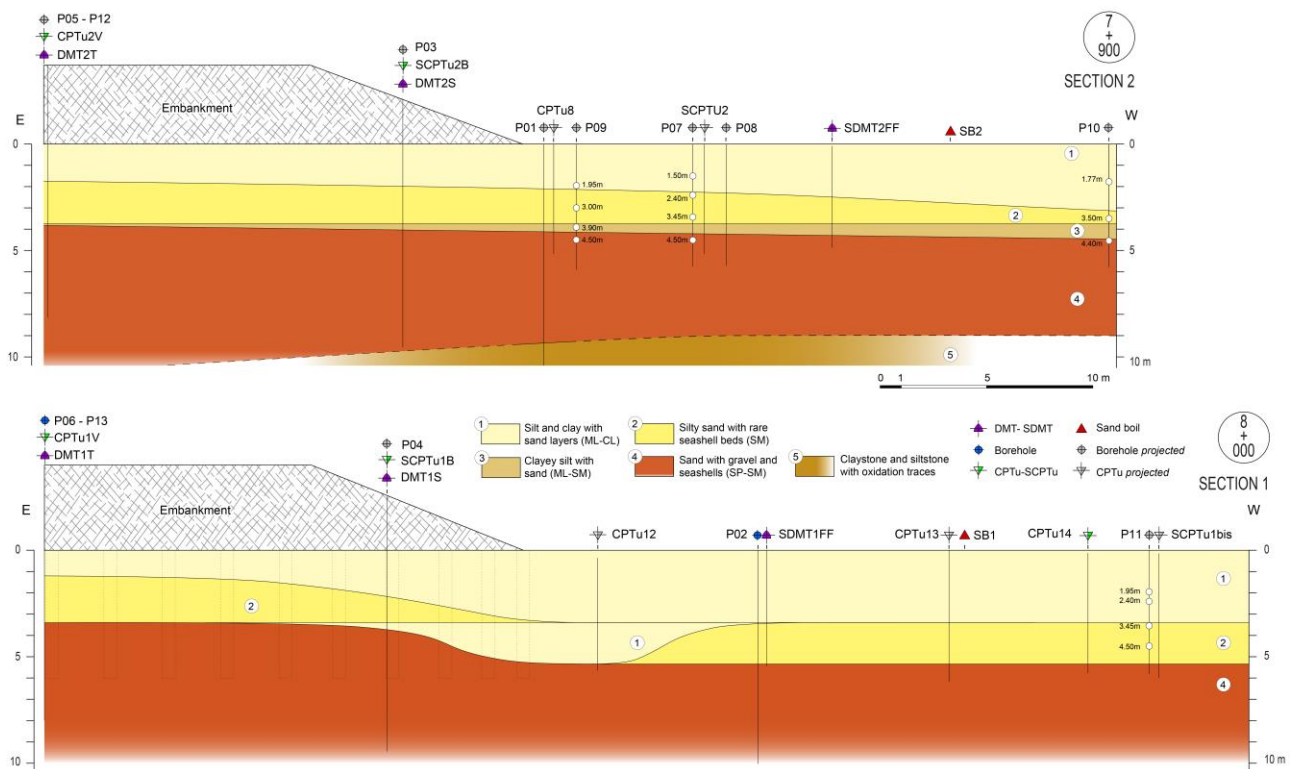
Fig. 4 Stratigraphic scheme of the successions involved in the liquefaction in the Briceño Bridge area showing the boreholes, the geotechnical tests (modified from Amoroso et al., 2020b) and the reconstructed lithological units across two sections (section 1 and section 2; see Fig. 1 for location).

229   *4.3 Grain-size*

230

231   The grain-size of the examined core samples ranges from almost pure sand to sandy silt (Fig. 5); the

232   silt fraction varies from 10 to 60%, but the amount of clay is always less than 10%. An increase in

233   grain size is observed with depth: finer samples characterize the shallow portion of the cores (at 1.5

234   to about 2 m depth below the ground level). From 2 to 4.5 m sands are fine to medium-grained (in

235   two samples a coarse-grained fraction is also present) and the silty fraction is less than 40% (with

236   the exception of sample P11_450, which is characterized by a higher amount of silt, about 50%).

237   The sand volcanoes are made up of fine sands, and the three examined samples perfectly overlap

238   despite belonging to different liquefaction sites. The amount of silt is around 30% and clay is less

239   than 5%.
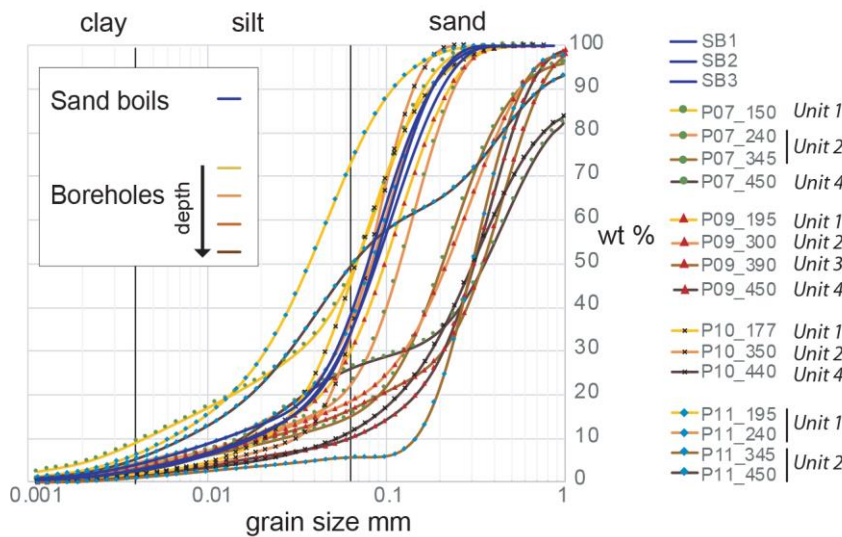
240

241   **Fig. 5** Cumulative grain-size distributions of examined samples from cores at different depths and

242   from sand blows (in blue).

243

244   The grain size analyses and the calculated index properties were then used to provide the USCS

245   classification (ASTM D2487-11, 2011), reported in Table 1. Samples from shallow unit 1 are sandy

246   silt (ML), whereas samples from deeper units 2 and 3 are silty sand (SM). The index properties

247   (Table 1) indicate a similar high fines content in both the silty sand (SM) layers (FC ≈ 17-53%), and

248   in the sand blows (FC ≈ 43-48%). The samples from the boreholes and the sand blows are well-

249   graded (i.e., they contain particles with a wide range of sizes), as shown by the coefficients of

250   curvature C and uniformity U. Atterberg limits confirmed that all the samples are non-plastic.

Samples	Description/Depth	FC (%)	D60 (mm)	D30 (mm)	D10 (mm)	U	C	USCS classification
P07_150	Section 2 - Borehole P07 1.50 m	55.64	0.0832	0.0324	0.0045	18.6	2.8	Sandy silt (ML)
P07_240	Section 2 - Borehole P07 2.40 m	27.41	0.1401	0.0814	0.0177	7.9	2.7	Silty sand (SM)
P07_345	Section 2 - Borehole P07 3.45 m	17.07	0.2502	0.1322	0.0263	9.5	2.7	Silty sand (SM)
P07_450	Section 2 - Borehole P07 4.50 m	27.24	0.4594	0.1245	0.0155	29.6	2.2	Silty sand (SM)
P09_195	Section 2 - Borehole P09 1.95 m	37.22	0.1182	0.0634	0.0163	7.3	2.1	Silty sand (SM)
P09_300	Section 2 - Borehole P09 3.00 m	20.52	0.2692	0.1256	0.0195	13.8	3.0	Silty sand (SM)
P09_390	Section 2 - Borehole P09 3.90 m	18.24	0.4101	0.2060	0.0210	19.5	4.9	Silty sand (SM)
P09_450	Section 2 - Borehole P09 4.50 m	11.62	0.3621	0.2072	0.0616	5.9	1.9	Poorly graded sand with silt (SP-SM)
P10_177	Section 2 - Borehole P10 1.77 m	56.00	0.0820	0.0457	0.0207	4.0	1.2	Sandy silt (ML)
P10_350	Section 2 - Borehole P10 3.50 m	46.69	0.0902	0.0597	0.0312	2.9	1.3	Silty sand (SM)
P10_440	Section 2 - Borehole P10 4.40 m	13.60	0.3867	0.1767	0.0527	7.3	1.5	Silty sand (SM)
P11_195	Section 1 - Borehole P11 1.95 m	80.03	0.0466	0.0210	0.0062	7.6	1.5	Silt with sand (ML)
P11_240	Section 1 - Borehole P11 2.40 m	45.51	0.0983	0.0530	0.0124	8.0	2.3	Silty sand (SM)
P11_345	Section 1 - Borehole P11 3.45 m	5.73	0.3458	0.2300	0.1450	2.4	1.1	Poorly graded sand with silt (SP-SM)
P11_450	Section 1 - Borehole P11 4.50 m	53.34	0.1213	0.0286	0.0074	16.5	0.9	Sandy silt (ML)
SB1	2016 sand boil	48.18	0.0936	0.0520	0.0122	7.7	2.4	Silty sand (SM)
SB2	2016 sand boil	43.42	0.1008	0.0571	0.0168	6.0	1.9	Silty sand (SM)
SB3	2016 sand boil	42.80	0.1059	0.0562	0.0178	5.9	1.7	Silty sand (SM)

251

252 **Table 1**. Index properties of the analyzed samples: FC is the fines content; D_{60}, D_{30}, and D_{10} are the
253 diameters of the 60th, 30th, and 10th percentiles of the grain size distribution; U is the coefficient of
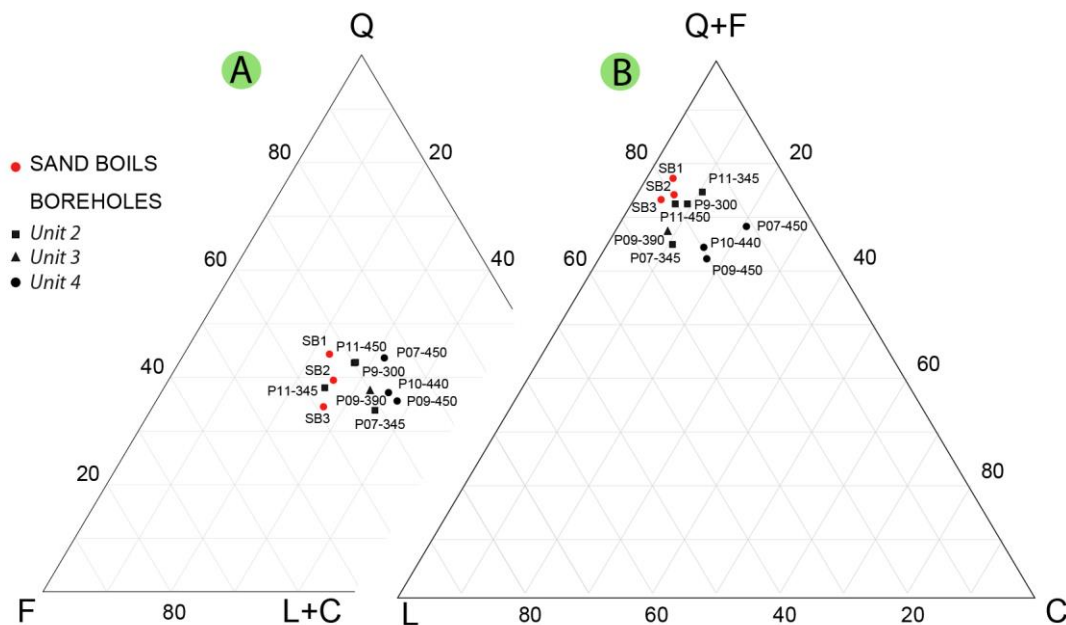254 uniformity; C is the coefficient of curvature.

255

256 *4.4 Composition of sands*

257 The results from the modal analyses are reported in Table 2 and in the ternary diagrams of Fig. 6.

258 The petrography under the optical microscope is shown in Fig. 7.

259

260

Fig. 6 Ternary diagrams Q,F, L+C and Q+F, L, C showing the composition of examined sands from cores (numbers refer to depth) and from liquefied sand boils (in red). Q, total quartz; F, total feldspars; L, siliciclastic lithic fragments; C, carbonate fragments.

In general, sands from the cores are made up of quartz (single crystal and polycrystalline) ranging from 28.0 to 37.3% of the bulk rock. Total feldspars range from 20 to 33% and consist largely of plagioclase and subordinately K-feldspar (orthoclase and microcline). Both quartz and feldspar grains are angular. Siliciclastic lithic fragments are made up primarily of volcanites (with microcrystalline groundmass with feldspar phenocrysts), spilites and serpentinites. Low-grade metamorphic rocks are minor components consisting of mica schist and phyllades. Sedimentary rocks include siltstones and shale. Siliciclastic lithics account for 9 to 21% of the whole rock.

Carbonate grains (6 to 16.3%) are made of bioclasts (benthic foraminifera, algae) (Fig. 7b), calcite spar and micritic grains. The amount of bioclasts is higher in the deeper samples (at depth of 4.5 m) and significantly decreases in the shallower samples (from 3.9 to 3.0 m depth).

Other significant components are micas, biotite, muscovite and chlorite, amphibole (mainly hornblende, green and brown), pyroxene and garnet. Glauconite is present in small amounts (less than 1%) in several samples. Opaque minerals (pyrite) and Fe-oxides are subordinate components. In all the studied sands, grains are angular to subangular.
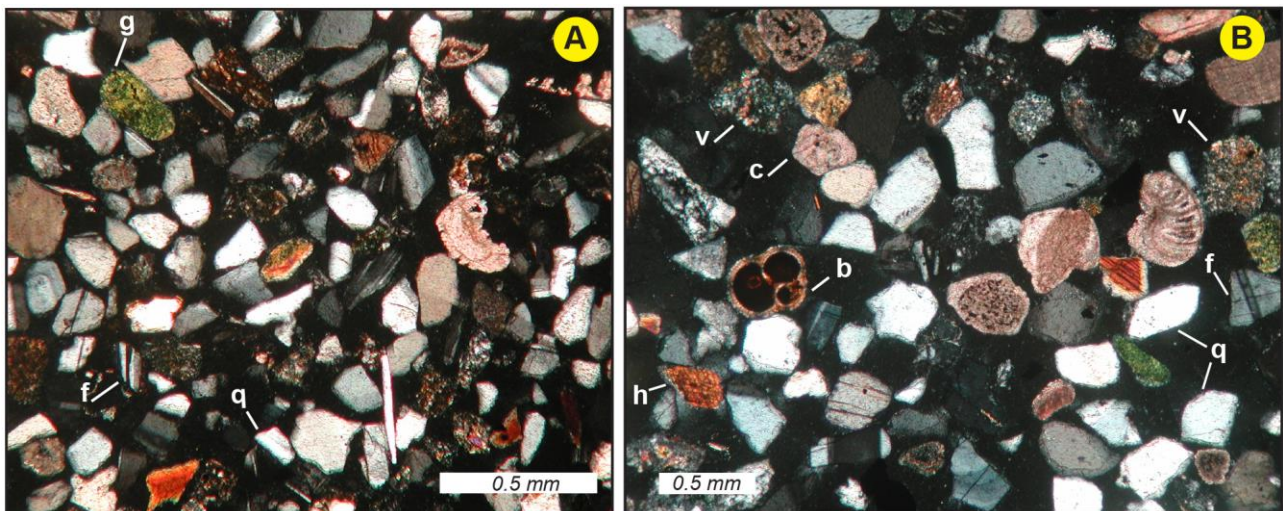
Fig. 7 Photomicrographs of the examined sands. A) sand blow (sample SB1) and B) core sample (P09_450), showing the main components, q: quartz, f: feldspars, b: bioclasts, c. calcite spar, v. volcanics, h. hornblende, g. glauconite. Transmitted light, crossed polars.

The composition of the sands indicate provenance from the erosion of the metamorphic/magmatic basement and volcanic rocks. Subordinate contributions are from sedimentary units (largely Miocene turbidite successions), in turn recycling basement lithotypes.

287 Samples from sand blows have a quite homogeneous composition with the same components
288 described for the core sands. Mainly based on the low amounts of carbonates, which consist largely
289 of bioclasts, the ejected sands show similarities with the shallower sands of unit 2. The similarity
290 among samples is assessed by the Ward distribution, calculated using all the petrographic
291 parameters (Fig. 8).
292
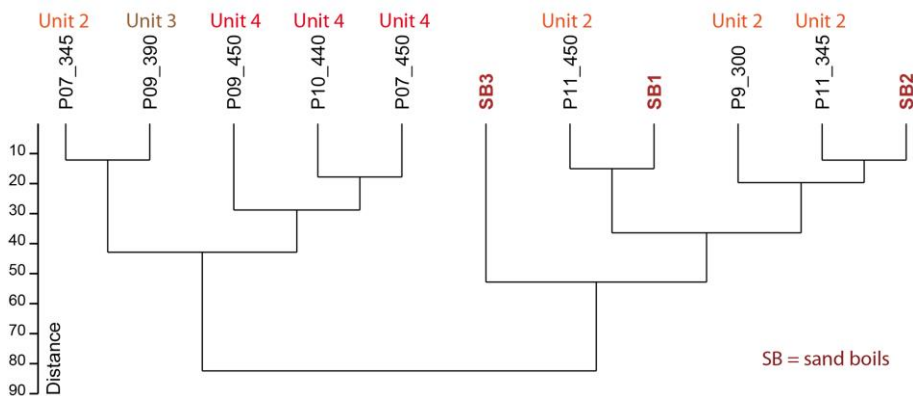
294 **Fig. 8** Dendrogram showing the distribution of samples calculated using all the petrographic
295 parameters. Ward's method. Similarity index: Euclidean.
296

		Boreholes								Sand boils		
		P07_345	P07_450	P09-300	P09_390	P09_450	P10_440	P11_345	P11_450	SB1	SB2	SB3
Q	Quartz single crystal	27,3	33,3	33,3	27,0	25,3	29,3	31,3	35,0	35,0	31,7	28,7
	Quartz polycrystalline	1,0	1,7	1,3	2,3	1,0	2,0	1,0	1,3	2,7	1,7	3,0
	Quartz in Rock fragment (r.f.)	0,3	0,3	1,0	1,0	1,7	0,0	1,7	1,0	1,3	0,3	0,7
F	K-feldspar single crystal	4,7	3,7	8,7	4,0	6,7	6,0	11,0	3,3	7,0	10,0	4,3
	K-feldspar in r.f.	0,3	0,0	0,0	0,3	0,0	0,0	0,0	0,0	0,0	0,3	0,0
	Plagioclase single crystal	20,3	16,3	16,3	19,3	14,3	17,0	20,7	22,7	21,7	19,0	31,3
	Plagioclase in r. f.	1,0	0,0	0,0	0,7	0,0	0,0	1,3	0,0	0,3	0,3	0,7
L	Metamorphite	1,7	1,0	1,0	0,0	0,7	1,0	0,7	1,3	2,7	2,0	1,0
	Volcanite	8,0	5,0	7,0	8,7	10,0	6,0	5,0	7,0	9,3	6,3	12,0
	Spilite	2,0	0,7	1,3	1,3	0,3	0,7	2,3	2,3	1,0	1,3	2,7
	Serpentinite	1,7	0,0	0,7	0,3	1,0	0,0	0,0	0,7	1,7	1,0	1,0
	Siltite	3,7	1,7	0,7	2,3	1,0	3,7	1,7	3,0	0,3	3,3	1,7
	Shale	4,0	1,0	5,0	7,0	3,3	5,7	4,0	3,7	1,3	3,0	2,7
C	Calcite spar	0,3	1,7	1,7	0,7	1,7	1,3	3,3	0,7	0,3	1,7	0,3
	Micrite	1,3	1,0	3,3	1,3	2,3	1,0	2,0	1,0	1,0	0,3	0,7
	Bioclast	7,0	13,7	2,3	4,7	9,7	10,7	3,7	4,3	2,3	3,0	3,0
	Mica and Chlorite	2,7	7,3	7,0	2,3	7,3	4,7	3,7	2,3	3,3	7,0	3,3
	Heavy mineral (unspecified)	2,3	2,3	1,0	2,7	3,0	2,0	1,0	1,3	1,7	1,7	0,3
	Heavy mineral (anfibol)	4,3	3,0	3,0	4,3	5,0	1,3	2,3	3,0	4,3	1,7	1,0
	Glauconite	1,0	0,0	0,3	0,3	0,0	1,0	0,3	0,3	0,3	0,3	0,7
	Fe-oxide	2,0	0,7	2,7	2,3	0,0	1,3	0,0	2,3	0,7	1,3	0,0
	Opaque	2,3	4,7	1,7	5,0	4,7	3,7	1,3	2,0	1,3	1,3	0,0
	Undetermined	0,7	1,0	0,7	2,0	1,0	1,7	1,7	1,3	0,3	1,3	1,0
		100%	100%	100%	100%	100%	100%	100%	100%	100%	100%	100%

298 **Table 2** Compositional modal analyses of examined sands (r.f., rock fragment). Composition is
299 determined based on transmitted-light spectroscopy of the 125–250 mm fraction.
300

301 **5. Discussion**

302

303 *5.1 Interpretation of the cored sequence*

304   The data from the 13 cores and from the geotechnical tests support the reconstruction of a detailed

305   stratigraphic scheme of Quaternary alluvial-marine sediments in the area and, in particular, of the

306   upper succession (from 0 to 5 m deep) in which the liquefiable layers are located (Fig. 4). Using the

307   described lithological characteristics and the sedimentary features recognizable from core pictures,

308   we may infer the following depositional environments:

309   - continental, fluvial-estuarine, for unit 1 and unit 5,

310   - marine to transitional fluvial, relatively-low energy, for units 2 and 3,

311   - marine, relatively-high energy, for unit 4.

312   Using as a reference the facies analyses of Di Celma et al. (2002), the studied sequence can be

313   attributed to the shallowing-upward segment of the last cyclothem, the sequence Tb6 of the

314   depositional model of Cantalamessa and Di Celma (2004).

315   The relatively large thickness of the continental deposits in the lower part of the sequence, unit 5,

316   which is at least 20 m-thick, suggests that this segment may represent the continental infill of the

317   fluvial paleo-valley of the Briceño River. The paleo-valley would have been cut during the sea level

318   lowstand corresponding to the Last Glacial Maximum. The valley was then flooded and filled

319   during the early phase of the Holocene transgression. The transition between units 4 and 5 may

320   represent the ravinement surface followed by a transgressive shoreface succession (unit 4). The

321   coarser marine sands of unit 4 may represent the exposed upper shoreface, and the following finer

322   marine sands of unit 2 would correspond to the shoreface environment migrating inland. Unit 3 may

323   represent the transitional marine-fluvial-estuarine facies. The topmost continental influx of unit 1

324   would indicate the last evolution of the sequence during the high stand, producing the final

325   regressive system tract made up of fluvial-estuarine mainly argillaceous sediments of the present-

326   day Briceño River**.**

327

328   *5.2 The source layer identification*

329   The petrographic composition of the sands allows us to discriminate the studied lithological units.

330   Sands of unit 4 are significantly richer in bioclasts and carbonate fragments relative to those of unit

331   2. The petrography of the liquefied sands that ejected to the surface as sand boils, compared with

332   that of buried sands, provides an important constraint in the recognition of the source layer. Based

333   on the compositional affinity, in particular the low amount of bioclasts and carbonate grains, as

334   shown by the Q+F, L, C ternary diagram (Fig. 6B), the sand boils were probably ejected from the

335   shallow silty sand level of unit 2, whereas the deeper coarser sands of unit 4 were not affected. The

336   affinity between the ejected sands and those of unit 2 is also confirmed considering the whole

337   petrographic composition illustrated in the Ward diagram (Fig. 8).

The grain-size results also support the petrographic data in attributing the ejected sands to unit 2. Although the grain-size alone can not provide precise indications of the source layer, in this case the deeper sands of unit 4, which are coarser than those of the sand boils, can not be the source layer even considering segregation processes during ejection. The attribution of the source layer for liquefaction to unit 2 is in agreement with the geotechnical assessment performed by Smith and Wissmann (2018) and Vera-Grunauer et al. (2019).

In general, this study seems to corroborate previous findings that earthquake-induced liquefaction phenomena are not restricted to clean sands and well-sorted deposits, but may affect sand layers with significant amount of non-plastic silt, as recently recognized in liquefied sands in the Po plain (Italy; Fontana et al., 2015, 2019; Amoroso et al. 2020b).

The dependence of liquefaction susceptibility with particle shape and roundness has been discussed in the literature (Garga and McKay, 1984; Vaid et al, 1985; Hird and Hassona, 1990; Ishihara 1993; Ashour and Norris, 1999; Ashmawy et al., 2003). In our case we observe a distinct angular shape of the grains suggesting that, as discussed by Ashmawy et al. (2003) this parameter is not necessarily an influencing factor for liquefaction, which depends primarily on the sediment texture, fabric and porosity.

6. Conclusions

- The study of the sands ejected at Rio Briceño valley (Ecuador) during the Mw 7.8 earthquake of April 2016 and the comparison with buried alluvial-marine Quaternary sediments, provided us with clues about the source layers identification.

- The composition and fabric characteristics, such as grain-size distribution, indicate that liquefaction processes affected mainly sand layers at depth of 2-4.5 m, and a relatively shallow source for the blowouts. The deeper coarser marine sands, characterized by higher amounts of carbonate grains, mainly bioclasts, were not affected by liquefaction.

- This study seems to corroborate previous findings that earthquake-induced liquefaction phenomena are not restricted to clean sands and well-sorted deposits, but may affect sand layers with significant amount of non-plastic silt.

REFERENCES

Alvarez, J. O., Schechter, D. S. (2017). Improving oil recovery in the Wolfcamp unconventional liquid reservoir using surfactants in completion fluids. Journal of Petroleum Science and Engineering, 157, 806-815.

Amoroso, S., Rollins, K.M., Wissmann, K., Minarelli, L. (2019). Estimation of lateral spreading by SPT, CPTU and DMT following the 2016 Mw7.8 Ecuador earthquake. Conference paper at 6th International Conference on Geotechnical and Geophysical Site Characterization. 7-11 September, 2020.

Amoroso, S., Rollins, K.M., Wissmann, K., Minarelli, L. (2020a). Estimation of lateral spreading by SPT, CPTU and DMT following the 2016 Mw7.8 Ecuador earthquake. Proceedings of the 6th International Conference on Geotechnical and Geophysical Site Characterization - ISC'6 Conference, 7-11 September 2020, Budapest, Hungary.

Amoroso, S., Rollins, K.M., Andersen, P., Gottardi, G., Tonni, L., García Martínez, M.F., Wissmann, K., Minarelli, L., Comina, C., Fontana, D., De Martini, P.M., Monaco, P., Pesci, A., Sapia, V., Vassallo, M., Anzidei, M., Carpena, A., Cinti, F., Civico, R., Coco, I., Conforti, D., Doumaz, F., Giannattasio, F., Di Giulio, G., Foti, S., Loddo, F., Lugli, S., Manuel, M.R., Marchetti, D., Mariotti, M., Materni, V., Metcalfe, B., Milana, G., Pantosti, D., Pesce, A., Salocchi, A.C., Smedile, A., Stefani, M., Tarabusi, G., Teza, G. (2020b). Blast-induced liquefaction in silty sands for full-scale testing of ground improvement methods: insights from a multidisciplinary study. Engineering Geology, 265, 17 pp, https://doi.org/10.1016/j.enggeo.2019.105437

Arribas, J., and Tortosa, A. (2003), Detrital modes in sedimenticlastic sands from first- order streams of the Iberian Range, Spain: the potential for sand generation of different sedimentary rocks: Sedimentary Geology, 159, p. 275–303.

Ashmawy, A., Sukumaran, B., Hoang, V. (2003). Evaluating the Influence of Particle Shape on Liquefaction Behavior Using Discrete Element Modeling. Proc. Offshore and Polar Engineering Conference.

ASTM D2487-11 (2011). Standard Practice for Classification of Soils for Engineering Purposes (Unified Soil Classification System).

Beauval, C., Marinière, J., Laurendeau, A., Singaucho, J.C., Viracucha, C., Vallée, M., Maufroy, E., Mercerat, D., Yepes, H., Ruiz, M., Alvarado, A. (2017). Comparison of observed ground motion attenuation for the 16 April 2016 Mw 7.8 Ecuador megathrust earthquake and its two largest aftershocks with existing ground motion prediction equations, Seismol. Res. Lett. 88(2A), pp. 287–299.

Cantalamessa, G., Di Celma, C., Bianucci, G., Carnevale, G., Coltorti, M., Delfino, M., G. Ficarelli, M. Moreno Espinosa, D. Naldini, P. Pieruccini, L. Ragaini, L. Rook, M. Rossi, G. Tito, D. Torre, G. Valleri, W. Lanini (2001). A new vertebrate fossiliferous site from the Late Quaternary at San José on the north coast of Ecuador: preliminary note. Journal of South American Earth Sciences, 14(3), 331-334.

Cantalamessa, G., Di Celma, C. (2004). Origin and chronology of Pleistocene marine terraces of Isla de la Plata and of flat, gently dipping surfaces of the southern coast of Cabo San Lorenzo (Manabı, Ecuador). Journal of South American Earth Sciences, 16(8), 633-648.

Chunga, K., Livio, F., Mulas, M., Ochoa-Cornejo, F., Besenzon, D., Ferrario, M.F., Michetti, A.M. (2018). Earthquake ground effects and intensity of the 16 April 2016 Mw 7.8 Pedernales, Ecuador, earthquake: implications for the source characterization of large subduction earthquakes. Bulletin of the Seismological Society of America, 108(6), pp. 3384-3397.

Di Celma, C., Ragaini, L., Cantalamessa, G., Curzio, P. (2002). Shell concentrations as tools in characterizing sedimentary dynamics at sequence-bounding unconformities: examples from the lower unit of the Canoa Formation (Late Pliocene, Ecuador). Geobios, 35, 72-85.

Ego, F., Sébrier, M., Lavenu, A., Yepes, H., Egues, A. (1996). Quaternary state of stress in the Northern Andes and the restraining bend model for the Ecuadorian Andes. Tectonophysics, 259(1-3), 101-116.

Fontana, D., Lugli, S., Dori, S. M., Caputo, R., Stefani, M. (2015). Sedimentology and composition of sands injected during the seismic crisis of May 2012 (Emilia, Italy): clues for source layer identification and liquefaction regime. Sedimentary Geology, 325, 158-167.

Fontana, D., Amoroso, S., Minarelli, L., Stefani, M. (2019). Sand Liquefaction Induced By a Blast Test: New Insights On Source Layer and Grain-Size Segregation Mechanisms (Late Quaternary, Emilia, Italy). Journal of Sedimentary Research, 89(1), 13-27.

438 Geotechnical Extreme Events Reconnaissance Association–Applied Technology Council (GEER-
439   ATC). 2016 "Earthquake Reconnaissance, Mw 7.8, April 16th, 2016, Muisne, Ecuador",
440   Nikolaou, S., X. Vera-Grunauer, and R. Gilsanz (Editors), Version 1b, 604 pp., 2016. doi:
441   10.18118/G6F30N.

442 Giona Bucci, M., Villamor, P., Almond, P., Tuttle, M., Stringer, M., Ries, W., Smith, C., Hodge,
443   M., Watson, M. (2018). Associations between sediment architecture and liquefaction
444   susceptibility in fluvial settings: the 2010–2011 Canterbury Earthquake Sequence, New Zealand.
445   Eng. Geol. 237, 181–197.

446 Gutscher, M. A., Malavieille, J., Lallemand, S., Collot, J. Y. (1999). Tectonic segmentation of the
447   North Andean margin: impact of the Carnegie Ridge collision. Earth and Planetary Science
448   Letters, 168(3-4), 255-270.

449 Hammer, Ø., Harper, D.A.T., Ryan, P.D. (2001). PAST: Paleontological statistics software package
450   for education and data analysis. Palaeontologia Electronica 4(1): 9pp. http://palaeo-
451   electronica.org/2001_1/past/issue1_01.htm

452 Jaillard, E., Ordoñez, M., Benitez, S., Berrones, G., Jiménez, N., Montenegro, G., Zambrano, I.
453   (1995). Basin development in an accretionary, oceanic-floored fore-arc setting: southern coastal
454   Ecuador during late Cretaceous-late Eocene time.

455 Jaillard, E., Benitez, S., Mascle, G. H. (1997). Les déformationspaléogenes de la zone d'avant-arc
456   sud-équatorienneen relation avec l'évolutiongéodynamique. Bulletin de la Société géologique de
457   France, 168(4), 403-412.

458 Kellogg, J. N., Vega, V., Stallings, T. C., Aiken, C. L. (1995). Tectonic development of Panama,
459   Costa Rica, and the Colombian Andes: constraints from global positioning system geodetic
460   studies and gravity. Special papers Geological Society of America, 75-75.

461 Lugli, S., Marchetti Dori, S., Fontana, D., (2007). Alluvial sand composition as a tool to unravelthe
462   Late Quaternary sedimentation of theModena Plain, northern Italy. In: Arribas,J., Critelli, S.,
463   Johnsson, M.J. (Eds.), Sedimentary Provenance and Petrogenesis: Perspectivesfrom Petrography
464   and Geochemistry. Geological Society of America SpecialPaper 420, pp. 57–72.

465 Maurer B.W., Green R.A., Wotherspoon L.M., Bastin S. (2019) The Stratigraphy of Compound
466   Sand Blows at Sites of Recurrent Liquefaction: Implications for Paleoseismicity Studies.
467   Earthquake Spectra: August 2019, 35(3), 1421-1440. https://doi.org/10.1193/041818EQS097M

468 Pedoja, K., Ortlieb, L., Dumont, J. F., Lamothe, M., Ghaleb, B., Auclair, M., Labrousse, B. (2006).
469   Quaternary coastal uplift along the Talara Arc (Ecuador, Northern Peru) from new marine
470   terrace data. Marine Geology, 228(1-4), 73-91.

471 Pedoja, K., Dumont, J. F., Lamothe, M., Ortlieb, L., Collot, J. Y., Ghaleb, B., Ghaleb, M. Auclair,
472   V. Alvarez, Labrousse, B. (2006). Plio-Quaternary uplift of the Manta Peninsula and La Plata
473   Island and the subduction of the Carnegie Ridge, central coast of Ecuador. Journal of South
474   American Earth Sciences, 22(1-2), 1-21.

475 Reynaud, C., Jaillard, É., Lapierre, H., Mamberti, M., Mascle, G. H. (1999). Oceanic plateau and
476   island arcs of southwestern Ecuador: their place in the geodynamic evolution of northwestern
477   South America. Tectonophysics, 307(3-4), 235-254.

478 Sheppard, G., (1930). The geology of South Western Ecuador. American Association of Petroleum
479   Geologists Bulletin 14, 263–309.

480 Smith, M.E., Wissmann, K. (2018). Ground improvement reinforcement mechanisms determined
481   for the Mw 7.8 Muisne, Ecuador, earthquake. In: 5th Geotechnical Earthquake Engineering and
482   Soil Dynamics Conference: Liquefaction Triggering, Consequences, and Mitigation - GEESDV
483   2018, Austin, Texas, June 10-13, 2018, GSP 290, pp. 286-294.

484 Trenkamp, R., Kellogg, J. N., Freymueller, J. T., Mora, H. P. (2002). Wide plate margin
485   deformation, southern Central America and northwestern South America, CASA GPS
486   observations. Journal of South American Earth Sciences, 15(2), 157-171.

487 Vera-Grunauer, X.F., Lopez-Zhindon, S., Ordonez-Rendon, J., Chavez-Abril, M.A. (2019).
488   Liquefaction case histories after the 2016 megathrust Pedernales earthquake in Ecuador. In: 7th
489   International Conference on Eartquake Geotechnical Engineering – 7 ICEGE, Rome, Italy, June,
490   17-20, 2019, pp. 805-820.

491 Wentz, F.J., van Ballegooy, S., Rollins, K.M., Ashford, S.A., Ol-sen, M.J. (2015). Large Scale
492   Testing of Shallow Ground Improvements using Blast-Induced Liquefaction", In: 6th
493   International Conference on Earthquake Geotechnical Engineering – 6 ICEGE, Christchurch,
494   New Zealand, Nov., 2-4, 2015.

495 Wissmann, K.J., van Ballegooy, S., Metcalfe, B.C., Dismuke, J.N., Anderson, C.K. (2015).
496   Rammed aggregate pier ground improve-ment as liquefaction method in sandy and silty soils",
497   In: 6th In-ternational Conference on Earthquake Geotechnical Engineering - 6ICEGE,
498   Christchurch, New Zealand, Nov., 2-4.

499 Ye, L., Kanamori, H., Avouac, J.P., Li, L., Cheung, K.F., Lay, T. (2016). The 16 April 2016, Mw
500   7.8 (Ms 7.5) Ecuador earthquake: a quasirepeat of the 1942 Ms 7.5 earthquake and partial re-
501   rupture of the 1906 Ms 8.6 Colombia–Ecuador earthquake. Earth Planet. Sci. Lett. 454, pp. 248–
502   258, 2016

503   Zuffa, G.G., (1985). Optical analyses of arenites: influence of methodology on compositional
504   results. In: Zuffa, G. (Ed.), Provenance of Arenites NATO ASI 148.
505   Dordrecht/Boston/Lancaster, D. Reidel Publishing Company, pp. 165–189.
506